

See discussions, stats, and author profiles for this publication at: <https://www.researchgate.net/publication/265912763>

# Oligonucleotide Flexibility Dictates Crystal Quality in DNA-Programmable Nanoparticle Superlattices

ARTICLE *in* ADVANCED MATERIALS · NOVEMBER 2014

Impact Factor: 17.49 · DOI: 10.1002/adma.201402548

CITATIONS

6

READS

36

9 AUTHORS, INCLUDING:



[Andrew J Senesi](#)

Northwestern University

24 PUBLICATIONS 838 CITATIONS

SEE PROFILE



[Byeongdu Lee](#)

Argonne National Laboratory

205 PUBLICATIONS 6,447 CITATIONS

SEE PROFILE



[Chung Hang Jonathan Choi](#)

The Chinese University of Hong Kong

18 PUBLICATIONS 1,811 CITATIONS

SEE PROFILE



[Kaylie L Young](#)

Northwestern University

14 PUBLICATIONS 721 CITATIONS

SEE PROFILE

# Oligonucleotide Flexibility Dictates Crystal Quality in DNA-Programmable Nanoparticle Superlattices

Andrew J. Senesi, Daniel J. Eichelsdoerfer, Keith A. Brown, Byeongdu Lee, Evelyn Auyeung, Chung Hang J. Choi, Robert J. Macfarlane, Kaylie L. Young, and Chad A. Mirkin\*

Superlattices composed of noble metal nanoparticles display considerable promise for the development of optical metamaterials,<sup>[1–5]</sup> and architectures with tunable permittivity,<sup>[3]</sup> permeability,<sup>[4]</sup> negative indices of refraction,<sup>[2,4,5]</sup> and even some with chiral<sup>[5,6]</sup> and active<sup>[7]</sup> responses have been explored. However, the realization of such architectures using nanoparticles has proven synthetically challenging because these structures typically require both high metallic volume fraction (approaching or exceeding 20%)<sup>[3,8]</sup> and large diameter particles (i.e., 30–100 nm). While superlattices have been formed using electrostatic,<sup>[9]</sup> entropic<sup>[10]</sup> and molecular interactions,<sup>[11]</sup> DNA-mediated assembly<sup>[12,13]</sup> offers unprecedented levels of control over the interparticle distance and superlattice symmetry. The development of metamaterials from DNA-nanoparticle superlattices, however, has been impeded by the difficulty in synthesizing periodic structures with suitably high metallic volume fractions, as they are more prone to kinetic jamming and often form non-crystalline arrangements regardless of annealing conditions. Here, we show that incorporating flexible spacers along with annealing DNA-nanoparticle systems close to their melting transitions improves crystalline quality in terms of domain size and microstrain. These insights allow for the crystallization of nanoparticle superlattices with up to 34% volume fraction, up from the previously reported maximum of 14%.<sup>[14]</sup> Importantly, this paper does not focus on metamaterials per se, but rather on the scientific underpinnings required to assemble large AuNPs into structures with high inorganic volume fractions.

In DNA-mediated nanoparticle assembly, nanoparticles are coated with a dense shell of double-stranded DNA that binds specific particles together using programmable hybridization. In

this sense, the particles act as “programmable atom equivalents” (PAEs), where each particle behaves as an “atom” with bonding behavior that can be tuned via the DNA interconnects. The synthetic tailorability afforded by DNA allows independent control over the superlattice connectivity and nanoparticle core, thereby enabling the design and synthesis of colloidal crystals with widely varying symmetry, scale, and composition.<sup>[14–19]</sup> While DNA-mediated assembly is a useful approach for spatially arranging noble metal nanoparticles, this method has not succeeded in forming crystals with short rigid DNA strands, especially for larger diameter particles.<sup>[14]</sup> This inability to crystallize large particles with small separations is likely a result of kinetic jamming behavior, which is often seen in colloidal systems<sup>[20]</sup> and may be related to the rigidity of the double-stranded DNA ligands.

Initial evidence for the importance of flexibility came from the observation that certain PAE systems which form amorphous aggregates when linked with fully duplexed DNA will crystallize if a single unpaired base is added to the DNA strands that link the particles.<sup>[12]</sup> Given that single-stranded DNA has a shorter persistence length than double-stranded DNA, this can be rationalized by considering that adding some degree of flexibility may be required to allow the packing of the inherently polydisperse particles into a regular lattice. Further, it is well known that the phase behavior of colloids depends on their range of interaction; long-range interactions result in a “softer” pair-potential that may allow for crystallization, while short-range interactions often result in jamming and gel formation.<sup>[21]</sup> Based on these observations, we hypothesize that adding flexibility to the DNA ligand could allow each strand to explore a wider space, thereby increasing the interaction range and decreasing jamming during PAE crystallization.

Herein, we explore the relationship between crystallization and linker flexibility by systematically adding various lengths of a flexible oligomer to the DNA ligand (**Figure 1**). Through annealing at different temperatures, we find that the highest quality crystals (defined here as crystals with the largest grain sizes and lowest microstrain as measured by X-ray diffraction) are formed at temperatures close to the melting temperature. Significantly, increasing ligand flexibility increases the temperature range under which crystallization occurs while simultaneously minimizing microstrain and maximizing domain size.

In a typical assembly experiment, PAE superlattices were observed by correlated synchrotron small-angle X-ray scattering (SAXS) and UV-vis spectroscopy (**Figure 2**), a set of measurements that allowed for the simultaneous determination of structural and thermodynamic information. Specifically, gold nanoparticles (AuNPs) were coated with a dense, oriented

Dr. A. J. Senesi,<sup>[†]</sup> Dr. D. J. Eichelsdoerfer,<sup>[†]</sup>  
Dr. K. A. Brown, Dr. C. H. J. Choi, Dr. R. J. Macfarlane,  
Dr. K. L. Young, Prof. C. A. Mirkin  
Department of Chemistry  
Northwestern University  
2145 Sheridan Rd., Evanston, IL 60208, USA  
E-mail: chadnano@northwestern.edu



Dr. A. J. Senesi, Dr. B. Lee  
X-ray Science Division  
Argonne National Laboratory  
9700 S. Cass Ave., Argonne, IL 60439, USA  
E. Auyeung, Prof. C. A. Mirkin  
Department of Materials Science and Engineering  
Northwestern University, 2220 Campus Dr.  
Evanston, IL 60208, USA

<sup>[†]</sup>These authors contributed equally to this work.

DOI: 10.1002/adma.201402548

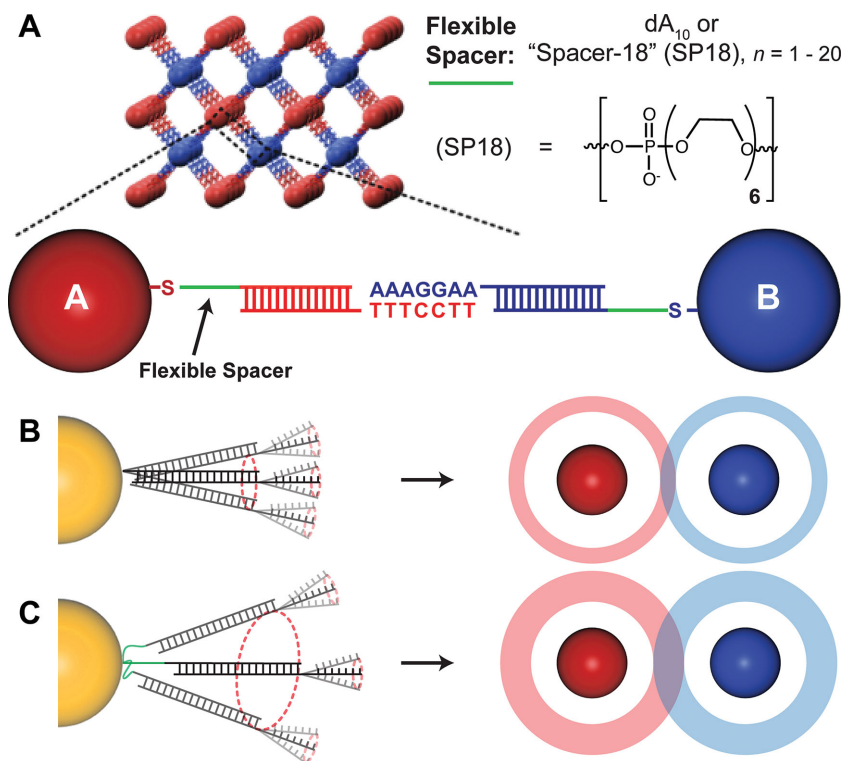


**Figure 1.** (A) Scheme showing DNA crystallization employing a flexible oligomer with hexaethylene glycol phosphate (Spacer-18) repeat units in the spacer region. We propose that the flexibility could increase the interaction range of PAEs, which is known to prevent jamming in colloidal systems. The successive addition of a flexible oligomer to the DNA ligand (from B to C) will allow the DNA strands greater conformational freedom, thereby increasing the volume in which the sticky end could be located and widening the interaction range.

monolayer of an oligomer composed of a thiolated "spacer" region (either a  $\text{dA}_{10}$  sequence or a hexaethylene glycol phosphate oligomer), an 18 DNA base duplexed region, a hexaethylene glycol phosphate monomer (or "flexor"), and an unpaired 7 DNA base "sticky end" (Figure 1A). A solution of these particles in phosphate buffered saline (0.5 M NaCl) was mixed with an equal concentration of a second particle species that had been coated with a similar oligomer with a complementary sticky end sequence. After mixing, the system was allowed to fully aggregate at room temperature, forming an amorphous material. The samples were subsequently annealed at various temperatures (the "annealing temperature") and for various times (the "annealing time"), typically 12 h. Annealing resulted in a variety of structural changes including a disorder-to-order transition, decrease in microstrain, and increase in grain size (vide infra); we note that our definitions of 'annealing temperature' and 'annealing time' refer to experimentally variable parameters and not transition temperatures associated with each structural change. Without lowering the temperature, the supernatant (including any free particles) was then removed from the aggregates. The supernatant particle concentration was determined by UV-vis spectroscopy to give the fraction of free particles, yielding a melting curve where each point was obtained from a distinct sample (Figure 2B). The aggregates were subsequently examined by SAXS (Figure 2C). Corroborating structural evidence was provided by transmission

electron microscope (TEM) imaging of samples embedded in silica,<sup>[22]</sup> a technique which preserves the configuration of the sample upon removal from solution.

As an initial experiment, we examined the effect of temperature on the crystallinity of a body centered cubic (BCC) system, comprised of 8.7 nm diameter AuNP cores. Melting and SAXS data are presented in Figure 2B and C, respectively. All the SAXS patterns correspond to BCC symmetry, with various degrees of ordering (Figure 2C). As the annealing temperature increases, the scattering peaks appear sharper and more defined, indicating that the samples are forming larger, more ordered crystallites.<sup>[24]</sup> Interestingly, the scattering spectra showed no change for annealing times between 15 min and 12 h (Figure S8, Supporting Information), indicating that structural changes occur at relatively short timescales (<15 min), and grain growth stagnates with a temperature dependent endpoint. In other words, the ability of a given PAE system to rearrange is governed by temperature. This stagnation has been observed in atomic systems of pure metals, alloys and ceramics, and is often attributed to grain boundary pinning, trenching and/or smooth grain boundary interfaces.<sup>[23]</sup> TEM imaging of PAE superlattices reveals segregation of outlier particles (ones with significantly different size or shape) at grain boundaries in addition to

many isolated crystals, which may contribute to this phenomenon (Figure S13, Supporting Information).

SAXS lineshape analysis was used to quantitatively examine annealing behavior and deconvolute the effects of domain size and microstrain. The integral breadth ( $\beta$ ) of each scattering peak is a measure of peak broadening resulting from a combination of grain size and defects, where decreasing  $\beta$  (i.e., sharper peaks) indicates more ordered structures.<sup>[24]</sup> As the temperature increases to approximately the melting temperature ( $T_m$ , defined as the temperature where the fraction of free particles equals the fraction of bound particles) under isochronal conditions,  $\beta^*$  (where \* indicates the first-order peak) continuously decreases and can be fit to a Hall sigmoidal curve (Figure 2D). To better understand the structural transformations during annealing, the effects of size and microstrain were deconvoluted using Williamson-Hall peak-shape analysis; size effects are independent of the scattering vector  $q$ , while microstrain effects are dependent on  $q$ . Stokes-Wilson strain broadening can be combined with Scherrer size broadening<sup>[24]</sup> to give the following relationship:

$$\beta \cos \theta = k\lambda / \tau + \eta \sin \theta \quad (1)$$

where  $\theta$  is the scattering angle,  $\lambda$  is the wavelength of X-ray radiation,  $\tau$  is the crystallite size,  $\eta$  is the apparent strain, and  $k$  is the shape factor, typically approximated as 0.9 for spherical

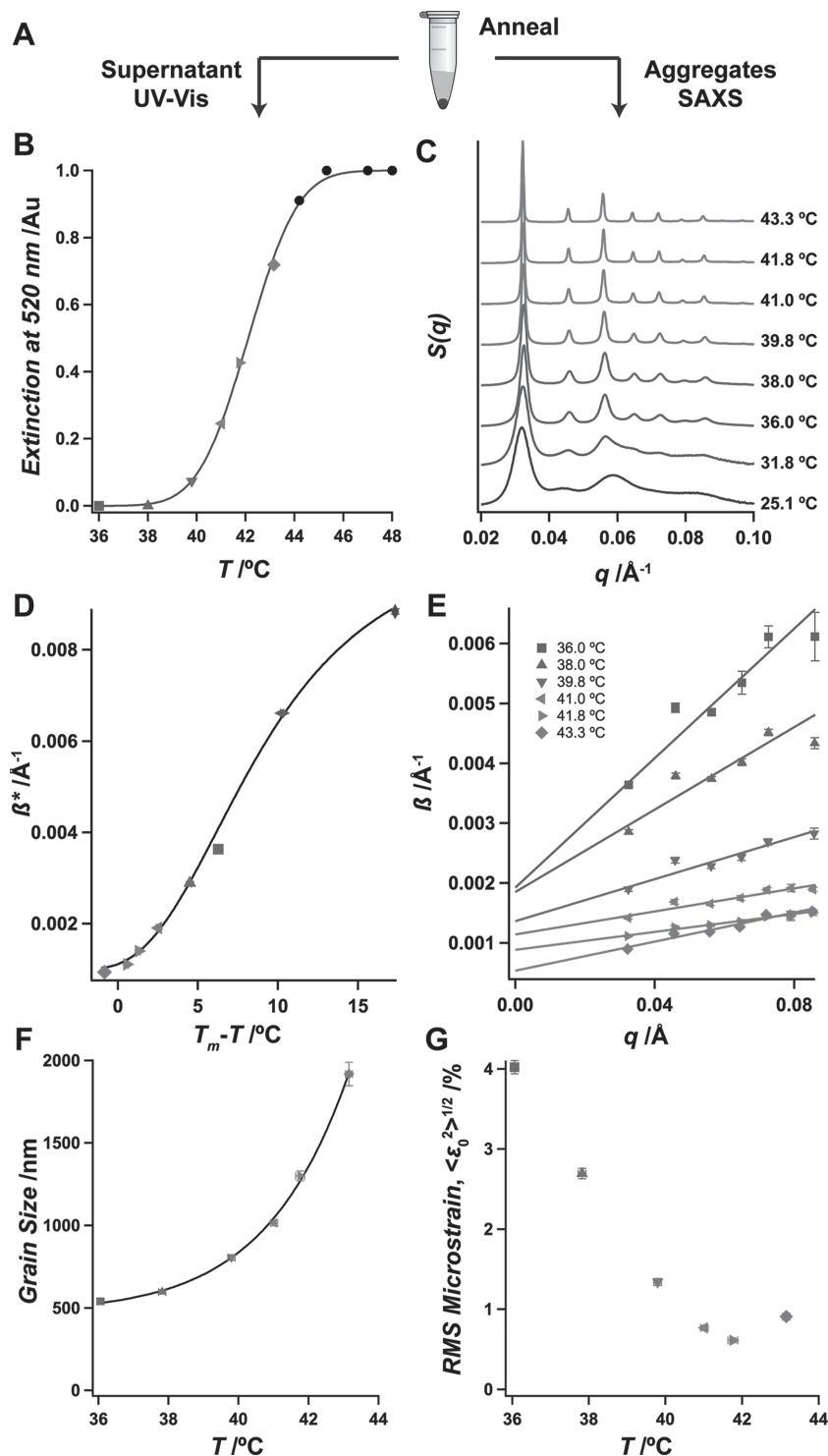


**Figure 2.** After annealing (A), the supernatant is separated from the aggregates to obtain a melting curve determined by UV-Vis spectroscopy, where each point is determined by a distinct sample annealed at a different temperature (B) (the curve is a best-fit sigmoidal), and the aggregates are examined by SAXS (C). The integral breadth ( $\beta^*$ ) of the first-order scattering peak is plotted as a function of  $T_m - T$  to give an “annealing curve” (D). Williamson-Hall analysis (E) can be used to deconvolute peak broadening arising from grain size (intercept, F) and microstrain (slope, G) by plotting  $\beta$  vs peak position ( $q$ ) for each scattering peak. Low-temperature annealing results in a decrease in microstrain while crystal growth occurs at higher temperatures. The colored data points from (B) correspond to the same samples and colors/markers in in (C-G).

crystallites.<sup>[24]</sup> Thus from a plot of  $\beta$  vs  $q$ , one can extract the size from the y-intercept and the strain from the slope.

The Williamson-Hall plot in Figure 2E shows a linear relationship, indicating that: i) microstrain is indeed isotropic for the crystals, and ii) for the purposes of determining grain size, the crystallites can be considered spherical. It is worth noting that shape or strain anisotropy aligned with a crystal zone axis would result in orientation-dependent peak broadening. Further, this analysis is sensitive to microstrain,  $\eta = \Delta a/a_{\text{mean}}$  (where  $a$  is the lattice parameter); uniform strains would manifest as a uniform shift in peak position. Two additional features are significant: as the annealing temperature increases for a given system, grain size increases (Figure 2F) and microstrain decreases (Figure 2G). Thus, at relatively low temperatures, defects are annealed out, while grain growth dominates the annealing process at higher temperatures. These phenomena can be understood from the tendency of the system to maximize hybridization events during annealing<sup>[16]</sup> through a temperature dependent de- and re-hybridization process,<sup>[14]</sup> which may have direct consequences for the grain growth stagnation noted above. After defect annealing, grain growth occurs, likely through coalescence and restructuring and/or by Ostwald-like ripening processes where particles migrate from smaller grains to larger grains.<sup>[25]</sup>

The finite temperature range in which a given PAE system will crystallize can be defined as its ‘annealing window’. The 8.7 nm AuNP system described above has a relatively large annealing window ( $>10$  °C); however, this range severely decreases as the nanoparticle size increases. For example, 38.1 nm diameter AuNPs with the same DNA sequence do not crystallize until the sample is annealed at 1 °C below  $T_m$  (Figure 3). We hypothesized that adding flexibility into the DNA system using a hexaethylene glycol phosphate group (Glen Research Corporation, ‘Spacer-18’, SP18) would widen the annealing window. Although SP18 contains a charged phosphate moiety, its persistence length in buffers with high ionic strength (e.g., 0.5 M NaCl used here) was found to be the same as polyethylene glycol<sup>[26]</sup> ( $L_p = 2.8$  Å) which is substantially less than single<sup>[27]</sup> ( $L_p = 7.5$  Å) or double<sup>[28]</sup> ( $L_p = 500$  Å) stranded DNA. Ligand flexibility was explored by adding various subunits of SP18 to the DNA at the flexible spacer region (Figure 1), annealing a series of samples at



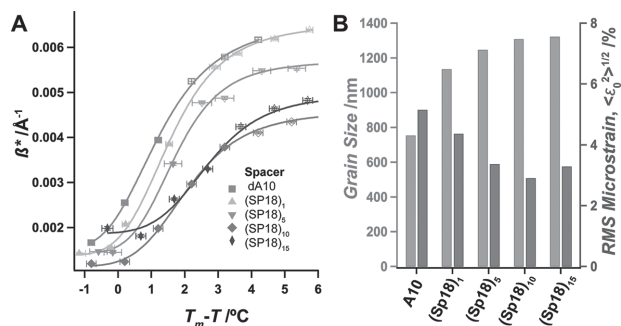


**Figure 3.** Adding flexibility to the DNA ligands connecting adjacent particles allows for the formation of higher quality crystals. (A) Annealing curves for 38.1 nm diameter AuNP cores with varying ligand flexibility plotted as a function of  $T_m - T$ , determined by SAXS. (B) Grain size and microstrain for each system at  $T_m$ , linearly interpolated from Williamson–Hall analysis of samples annealed just below and just above  $T_m$ .

various temperatures near  $T_m$ , and examining the structures by SAXS. The effect of adding the flexible spacer to the DNA sequence can clearly be seen in the annealing curves (Figure 3A, see Figure S3 and S4 in the Supporting Information for melting and SAXS data, respectively). As up to 10 SP18 units are added to the spacer region, the annealing curves broaden and shift to lower temperatures relative to  $T_m$ . Grain size and microstrain for each sample type at  $T_m$  were compared by linearly interpolating data points of samples annealed just above and just below the melting temperature, using Williamson–Hall analysis (Figure 3B). Generally, the grain size increases monotonically with flexibility while microstrain decreases. However, for samples with 15 SP18 units, an increase in microstrain was observed, and at 20 SP18 units, two phases could be distinguished consisting of crystal regions surrounded by an amorphous phase (Figure S12 and S13, Supporting Information). This could be explained in light of the earlier observation that outlier particles will segregate at grain boundaries (Figure S13, Supporting Information) coupled with the fact that larger diameter particles are generally more polydisperse.

The flexible SP18 spacers could have several effects. First, the SP18 results in a denser DNA shell compared to a dA<sub>10</sub> spacer,<sup>[29]</sup> possibly allowing more polyvalent interparticle interactions during annealing. Second, the increased flexibility allows polydisperse particles to pack into a regular array. Third, flexible ligands should be able to explore a larger volume surrounding the particle (Figure 1B,C), thereby widening the interaction pair potential. In addition, the local concentration of DNA sticky ends would decrease, which should depress the melting temperature. Indeed, as ligand flexibility increases, the melting temperature decreases (Figure S2, Supporting Information). It should be noted that this is not just an effect of ligand length; the dA<sub>10</sub>, (SP18)<sub>1</sub>, and (SP18)<sub>5</sub> systems all have similar lattice parameters, yet the increased flexibility widens the annealing window by ca. 1.5 °C. Furthermore, this is not solely an effect of the width of the melting transition. The same data plotted as  $\beta$  vs the singlet fraction, or the ratio of free over total particles, clearly shows a decrease in  $\beta$  with increasing additions of SP18 up to 10 subunits (Figure S5, Supporting Information). Thus, we postulate that flexibility itself is a major factor in the increased ability of the system to crystallize. Similar to

colloidal hard-sphere packing, longer interparticle interactions will widen and thus soften the pair potential, which is known to decrease jamming for colloidal systems.<sup>[21]</sup>

Using the principles outlined above, we next examined the crystallization of PAEs with larger diameter cores, up to approximately 100 nm in diameter (Figure 4). The range of the annealing window for each system can be found in Figure 4H. By using a (SP18)<sub>10</sub> flexible spacer, 58.6 and 77.5 nm diameter AuNPs crystallized at approximately  $T_m$  and 0.5 °C above  $T_m$ , respectively (Figure S9 and S10, Supporting Information). Note,  $T_m$  is defined as the temperature at which the fraction of free particles equals the fraction of bound particles; thus a sample may be annealed slightly above  $T_m$ , though a significant fraction of particles will dissociate from the crystals. For this spacer length, PAEs with 99.9 nm diameter AuNP cores remained disordered at all temperatures that were thermodynamically stable; crystallization was not observed until longer (SP18)<sub>20</sub> spacers were used, and even then not until almost 1 °C above  $T_m$  (Figure S11, Supporting Information).

While a variety of metamaterials designs have been proposed using noble metal colloidal building blocks, all rely on the plasmonic coupling between adjacent particles. For two particles, coupling is predicted to occur when the gap/diameter ratio is less than 0.5.<sup>[30]</sup> It is therefore expected that interesting plasmonic behavior will be present in PAE materials with these gap/diameter ratios  $<0.5$ , which for a BCC crystal occurs at ca. 20% volume fraction (Figure 4I). It should also be noted that higher volume fractions result in greater coupling, thereby enhancing plasmonic activity, which here has been achieved using PAEs with approximately greater than 40 nm diameter cores and up (Figure 4I and Table S3, Supporting Information). Additionally, one can estimate the range of volume fractions over which the superlattice is expected to have a photonic bandgap in the visible range by using results from the photonic crystal community and tabulated values of refractive indices of gold and water (blue band Figure 4I – for details see Supporting Information). While tuning ligand flexibility allows crystallization of these larger diameter PAEs in the regime expected to exhibit photonic and plasmonic effects, the annealing of systems within a narrow  $<1$  °C window is challenging. To mitigate these difficulties, samples were slowly cooled through  $T_m$  at a rate of 10 °C/hr,<sup>[19]</sup> which allowed for the reliable crystallization of PAEs with high yield (Figure 4A). Thus, appropriate ligand design and control over annealing conditions allows a wider range of particle diameter/volume fraction crystals to be synthesized (Figure 4I), which will in turn enable the development of nanoparticle superlattice based metamaterials.

In conclusion, DNA ligand flexibility expands the annealing window of PAEs, likely by widening and softening the interparticle interaction potential. Further, by studying the evolution of domain size and microstrain, we showed that annealing at low temperatures (relative to  $T_m$ ) removes defects, while grain growth primarily occurs at temperatures closer to  $T_m$ . These results allow one to drastically increase the maximum inorganic core volume fraction of PAE crystals (up to 34% is shown here, compared to 14% demonstrated previously<sup>[14]</sup>) and employ PAEs with core diameters up to 100 nm. Looking forward, these new capabilities may enable the realization of

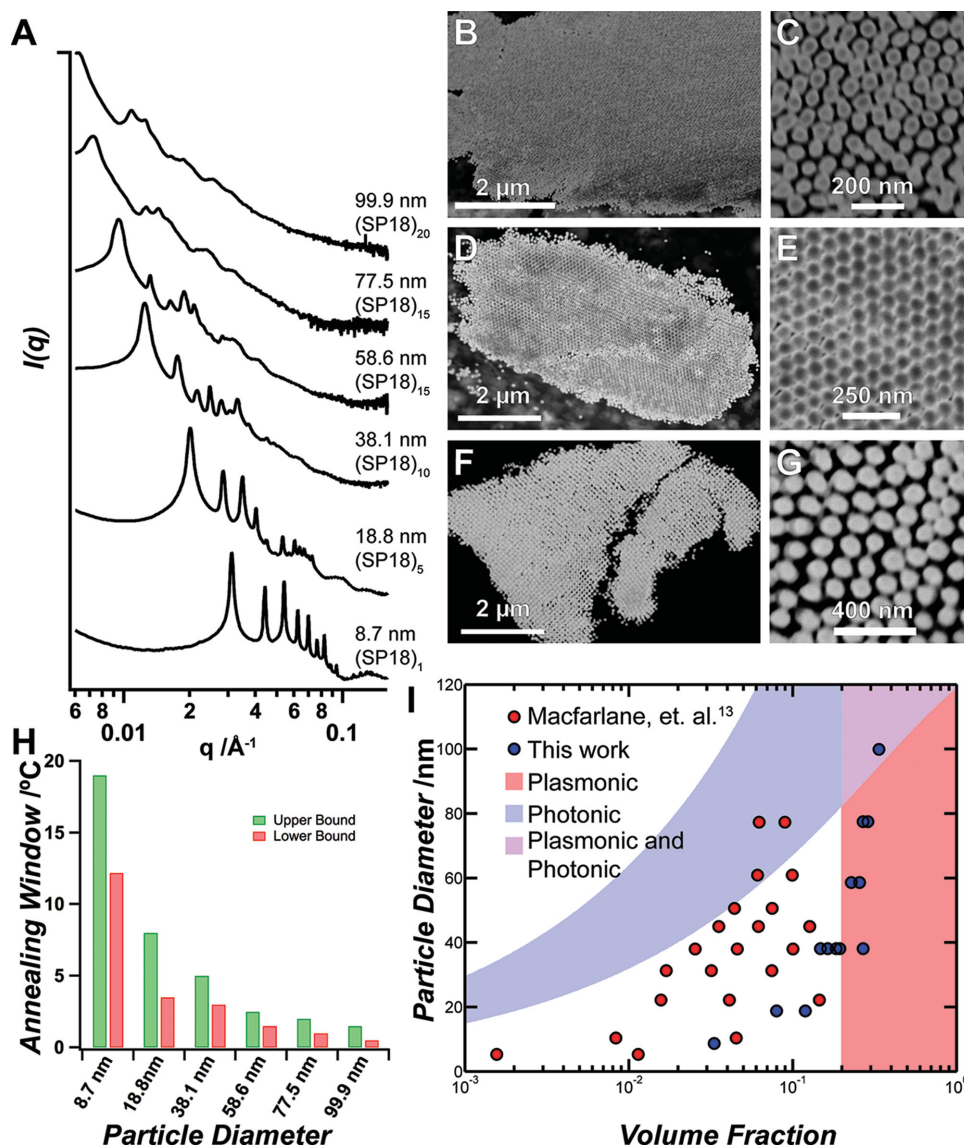


**Figure 4.** The use of flexible DNA ligands enables PAE crystal formation using larger diameter particles with higher noble metal volume fraction. (A) SAXS patterns for PAE samples employing varying diameter AuNP cores. (B–G) TEM images at low (B,D,F) and high (C,E,G) magnification show PAE crystals with large particles (58.6, 77.5, 99.9 nm core diameters, respectively). (H) Plot showing that the annealing window decreases with increasing particle diameter. Because of the discrete nature of our experiments, the annealing window is listed with an upper and lower bound. (I) Scatter plot depicting the crystals that have been synthesized in terms of their volume fractions and particle diameters. Notably, crystals reported herein (blue) extend beyond prior results (red) into the regime where plasmonic effects are expected to be important and even into the region where both plasmonic and photonic effects overlap.

PAE crystals as plasmonic metamaterials, and while this study employed AuNPs as a model system, these results should be applicable to other optically active materials such as Ag or semiconductor nanocrystals. While the size of the superlattices obtained herein is relatively modest ( $\mu\text{m}$ -sized), it is conceivable that they could be used to seed the growth of larger crystals, similar to bulk materials such as silicon, or grown as poly- or single-crystalline thin films<sup>[17,18]</sup> at the wafer scale. The results presented herein provide a significant advance in our understanding of PAE annealing behavior, and will allow future investigations into the role of plasmons in the optical behavior of these collective systems.

## Experimental Section

**Nanoparticle Crystallization:** PAE synthesis and purification were carried out using literature procedures described extensively elsewhere.<sup>[17,31]</sup> See also the main text. Further information can be found in the Supporting Information, including all DNA sequences, concentrations, and linker to NP molar ratios.

**Small-Angle X-ray Scattering (SAXS):** SAXS experimental details and lattice parameter calculations can be found in the Supporting Information.

**Transmission Electron Microscopy:** PAE crystals were embedded in silica using literature procedures.<sup>[22]</sup> Samples were visualized by simple drop-casting and using a resin-embedding and sectioning method.<sup>[22]</sup> All the images were acquired on a Hitachi HD-2300 instrument in z-contrast mode.

## Supporting Information

Supporting Information is available from the Wiley Online Library or from the author.

## Acknowledgements

This material is based upon work supported by the AFOSR Awards FA9550-11-1-0275 and FA9550-12-1-0141. D.J.E., E.A. and K.L.Y. acknowledge the Department of Defense and AFOSR for a National Defense Science and Engineering Graduate (NDSEG) Fellowship, 32 CFR 168a. K.A.B. gratefully acknowledges support from Northwestern University's International Institute for Nanotechnology. C.H.J.C. acknowledges a postdoctoral research fellowship from The Croucher Foundation. The SAXS experiments were carried out at Sector 5-ID of the DuPont-Northwestern-Dow Collaborative Access Team and Sector 12-ID-B at the Advanced Photon Source. Use of the Advanced Photon Source at Argonne National Laboratory was supported by the U.S. Department of Energy, Office of Science, Office of Basic Energy Sciences, under Contract No. DE-AC02-06CH11357. The TEM work was performed at the EPIC facility of the NU Atomic and Nanoscale Characterization Experimental Center (NUANCE) at Northwestern University.

Received: June 9, 2014

Revised: August 6, 2014

Published online: September 22, 2014

- [1] K. J. Stebe, E. Lewandowski, M. Ghosh, *Science* **2009**, 325, 159.
- [2] C. Rockstuhl, F. Lederer, C. Etrich, T. Pertsch, T. Scharf, *Phys. Rev. Lett.* **2007**, 99, 017401.
- [3] a) S. Campione, S. Steshenko, M. Albani, F. Capolino, *Opt. Express* **2011**, 19, 26027; b) K. L. Young, M. B. Ross, M. G. Blaber, M. Rycenga, M. R. Jones, C. Zhang, A. J. Senesi, B. Lee, G. C. Schatz, C. A. Mirkin, *Adv. Mater.* **2014**, 26, 653.
- [4] H. Alaeian, J. A. Dionne, *Opt. Express* **2012**, 20, 15781.
- [5] V. Yannopapas, *Appl. Phys. A* **2007**, 87, 259.
- [6] a) C.-L. Chen, P. Zhang, N. L. Rosi, *J. Am. Chem. Soc.* **2008**, 130, 13555; b) A. Kuzyk, R. Schreiber, Z. Fan, G. Pardatscher, E.-M. Roller, A. Högele, F. C. Simmel, A. O. Govorov, T. Liedl, *Nature* **2012**, 483, 311.
- [7] a) P. A. Kosyrev, A. Yin, S. G. Cloutier, D. A. Cardimona, D. Huang, P. M. Alsing, J. M. Xu, *Nano Lett.* **2005**, 5, 1978; b) J. A. Bossard, X. Liang, L. Li, S. Yun, D. H. Werner, B. Weiner, T. S. Mayer, P. F. Cristman, A. Diaz, I. C. Khoo, *IEEE Trans. Antennas Propag.* **2008**, 56, 1308; c) R. Pratibha, K. Park, I. I. Smalyukh, W. Park, *Opt. Express* **2009**, 17, 19459.
- [8] J. Dintinger, S. Mühlig, C. Rockstuhl, T. Scharf, *Opt. Mater. Express* **2012**, 2, 269.
- [9] a) M. E. Leunissen, C. G. Christova, A.-P. Hynninen, C. P. Royall, A. I. Campbell, A. Imhof, M. Dijkstra, R. van Roij, A. van Blaaderen, *Nature* **2005**, 437, 235; b) A. M. Kalsin, M. Fialkowski, M. Paszewski, S. K. Smoukov, K. J. M. Bishop, B. A. Grzybowski, *Science* **2006**, 312, 420; c) Z. Tang, Z. Zhang, Y. Wang, S. C. Glotzer, N. A. Kotov, *Science* **2006**, 314, 274.
- [10] a) S. Asakura, F. Oosawa, *J. Chem. Phys.* **1954**, 22, 1255; b) K. L. Young, M. R. Jones, J. Zhang, R. J. Macfarlane, R. Esquivel-Sirvent, R. J. Nap, J. Wu, G. C. Schatz, B. Lee, C. A. Mirkin, *Proc. Natl. Acad. Sci. USA* **2012**, 109, 2240; c) E. V. Shevchenko, D. V. Talapin, N. A. Kotov, S. O'Brien, C. B. Murray, *Nature* **2006**, 439, 55.
- [11] a) C. J. Kiely, J. Fink, M. Brust, D. Bethell, D. J. Schiffrin, *Nature* **1998**, 396, 444; b) Y. Zhao, K. Thorkelsson, A. J. Mastroianni, T. Schilling, J. M. Luther, B. J. Rancatore, K. Matsunaga, H. Jinnai, Y. Wu, D. Poulsen, J. M. J. Frechet, A. P. Alivisatos, T. Xu, *Nature Mater.* **2009**, 8, 979; c) C.-L. Chen, N. L. Rosi, *Angew. Chem. Int. Ed.* **2010**, 49, 1924.
- [12] S. Park, A. Lytton-Jean, B. Lee, S. Weigand, G. C. Schatz, C. A. Mirkin, *Nature* **2008**, 451, 553.
- [13] a) D. Nykpanchuk, M. Maye, D. van der Lelie, O. Gang, *Nature* **2008**, 451, 549; b) R. J. Macfarlane, M. N. O'Brien, S. H. Petrosko, C. A. Mirkin, *Angew. Chem. Int. Ed.* **2013**, 52, 5688; c) C. A. Mirkin, R. Letsinger, R. Mucic, J. Storhoff, *Nature* **1996**, 382, 607; d) A. P. Alivisatos, K. P. Johnsson, X. Peng, T. E. Wilson, C. J. Loweth, M. P. Bruchez Jr, P. G. Schultz, *Nature* **1996**, 382, 609.
- [14] R. J. Macfarlane, M. R. Jones, A. J. Senesi, K. L. Young, B. Lee, J. Wu, C. A. Mirkin, *Angew. Chem. Int. Ed.* **2010**, 49, 4589.
- [15] a) M. R. Jones, R. J. Macfarlane, B. Lee, J. Zhang, K. Young, A. J. Senesi, C. A. Mirkin, *Nat. Mater.* **2010**, 9, 913; b) C. Zhang, R. J. Macfarlane, K. L. Young, C. H. J. Choi, L. Hao, E. Auyeung, G. Liu, X. Zhou, C. A. Mirkin, *Nat. Mater.* **2013**, 12, 741; c) Y. Kim, R. J. Macfarlane, C. A. Mirkin, *J. Am. Chem. Soc.* **2013**, 135, 10342; d) R. J. Macfarlane, M. R. Jones, B. Lee, E. Auyeung, C. A. Mirkin, *Science* **2013**, 341, 1222.
- [16] R. J. Macfarlane, B. Lee, M. R. Jones, N. Harris, G. C. Schatz, C. A. Mirkin, *Science* **2011**, 334, 204.
- [17] A. J. Senesi, D. J. Eichelsdoerfer, R. J. Macfarlane, M. R. Jones, E. Auyeung, B. Lee, C. A. Mirkin, *Angew. Chem. Int. Ed.* **2013**, 52, 6624.
- [18] S. L. Hellstrom, Y. Kim, J. S. Fkonas, A. J. Senesi, R. J. Macfarlane, C. A. Mirkin, H. A. Atwater, *Nano Lett.* **2013**, 13, 6084.
- [19] E. Auyeung, T. I. N. G. Li, A. J. Senesi, A. L. Schmucker, B. C. Pals, M. O. de la Cruz, C. A. Mirkin, *Nature* **2014**, 505, 73.
- [20] V. J. Anderson, H. Lekkerkerker, *Nature* **2002**, 416, 811.
- [21] a) M. G. Noro, D. Frenkel, *J. Chem. Phys.* **2000**, 113, 2941; b) P. J. Lu, E. Zaccarelli, F. Ciulla, A. B. Schofield, F. Sciortino, D. A. Weitz, *Nature* **2008**, 453, 499; c) A. Yethiraj, A. van Blaaderen, *Nature* **2003**, 421, 513; d) E. Sanz, M. E. Leunissen, A. Fortini, A. van Blaaderen, M. Dijkstra, *J. Phys. Chem. B* **2008**, 112, 10861.
- [22] E. Auyeung, R. J. Macfarlane, C. H. J. Choi, J. I. Cutler, C. A. Mirkin, *Adv. Mater.* **2012**, 24, 5181.
- [23] a) K. Barmak, E. Eggeling, D. Kinderlehrer, R. Sharp, S. Ta'asan, A. D. Rollett, K. R. Coffey, *Prog. Mater. Sci.* **2013**, 58, 987; b) E. A. Holm, S. M. Foiles, *Science* **2010**, 328, 1138; c) E. Rabkin, *J. Mater. Sci.* **2005**, 40, 875.
- [24] a) R. L. Snyder, J. Fiala, H. J. DBunge, *Defect and Microstructure Analysis by Diffraction*, Oxford University Press, New York **1999**; b) E. J. Mittermeijer, U. Welzel, *Z. Kristallogr.* **2008**, 223, 552; c) C. Weidenthaler, *Nanoscale* **2011**, 3, 792.
- [25] J. Storhoff, A. Lazarides, R. Mucic, C. A. Mirkin, R. Letsinger, G. Schatz, *J. Am. Chem. Soc.* **2000**, 122, 4640.
- [26] Z. Tong, A. Mikheikin, A. Krasnoslobodtsev, Z. Lv, Y. L. Lyubchenko, *Methods* **2013**, 60, 161.
- [27] a) S. B. Smith, Y. Cui, C. Bustamante, *Science* **1996**, 271, 795; b) B. Tinland, A. Pluen, J. Sturm, G. Weill, *Macromolecules* **1997**, 30, 5763.
- [28] a) P. J. Hagerman, *Annu. Rev. Biophys. Biophys. Chem.* **1988**, 17, 265; b) S. B. Smith, L. Finzi, C. Bustamante, *Science* **1992**, 258, 1122.
- [29] S. J. Hurst, A. K. R. Lytton-Jean, C. A. Mirkin, *Anal. Chem.* **2006**, 78, 8313.
- [30] P. Jain, W. Huang, M. El-Sayed, *Nano Lett.* **2007**, 7, 2080.
- [31] H. Hill, C. A. Mirkin, *Nat. Protoc.* **2006**, 1, 324.